Supporting Information

Two-Step Electrochemical Oxidation Enables Synergistic Fe^{3+} Doping and PO_4^{3-} Modification of Nickel-Based Catalysts for Efficient Oxygen Evolution

Zhiheng He,[a] Wenxuan Li,[a] Runyu Jin,[a] Xiaotong Mao,[a] Senyuan Li,[a] Ke Tang,[a] Wenyu Huang,[b] Fangyan Xie,[b] Jian Chen,[b] Nan Wang,[a] Yanshuo Jin,*[a] and Hui Meng*[a]

a Siyuan Laboratory, Guangzhou Key Laboratory of Vacuum Coating Technologies and New Energy Materials, Guangdong Provincial Engineering Technology Research Center of Vacuum Coating Technologies and New Energy Materials, Guangdong Provincial Key Laboratory of Nanophotonic Manipulation, Department of Physics, Jinan University, Guangzhou, Guangdong, 510632 P.R. China

b Instrumental Analysis & Research Center, Sun Yat-sen University, Guangzhou, Guangdong, 510275 P.R. China

Author Information

Corresponding Author

jinyanshuo@email.jnu.edu.cn (Yanshuo Jin); tmh@jnu.edu.cn (Hui Meng).

Experimental section：

Synthesis of (Fe^{3+}, PO_4^{3-})-$Ni(OH)_2$/NiOOH: Pretreatment of the nickel mesh: Cut the nickel mesh into 1 × 1 cm^2 electrodes. Prepare a 1 mol/L KOH solution: Dissolve 66 g of KOH granules (85% purity) in 1 L of deionized water. Prepare a 10 mmol/L $FeCl_3$ solution: Dissolve 1.62 g of $FeCl_3 \cdot 6H_2O$ in 1 L of deionized water. Prepare 1 mol/L KOH + x mmol/L $FeCl_3$ solutions (x = 0.05, 0.1, 0.2) using the dilution method. For example: Mix 1 mL of 10 mmol/L $FeCl_3$ solution with 99 mL of 1 mol/L KOH solution to obtain a 1 mol/L KOH + 0.1 mmol/L $FeCl_3$ electrolyte. Place the Ni electrode in this electrolyte and perform cyclic voltammetry (CV) testing using a CHI 660 electrochemical workstation. Set the potential window to 1.0–1.4 V (vs. RHE), the scan rate to 50 mV/s, and the number of scan segments to 1000. After testing, thoroughly rinse the electrode with deionized water to remove residual electrolyte. Prepare a 100 mmol/L KH_2PO_4 solution: Dissolve 13.81 g of KH_2PO_4 in 1 L of deionized water. Prepare 1 mol/L KOH + x mmol/L $FeCl_3$ solutions (x = 1, 5, 10) using the dilution method. For example: Mix 1 mL of 100 mmol/L KH_2PO_4 solution with 19 mL of 1 mol/L KOH solution to obtain a 1 mol/L KOH + 5 mmol/L KH_2PO_4 electrolyte. Place the Ni electrode from the previous step back into this newly prepared electrolyte and perform cyclic voltammetry (CV) testing using a CHI 660 electrochemical workstation. Set the potential window to 1.0–1.4 V (vs. RHE), the scan rate to 50 mV/s, and the number of scan segments to 100. After the test, thoroughly rinse the electrode with deionized water to remove residual electrolyte.

Characterization: X-ray photoelectron spectroscopy (XPS, Thermo Fisher Scientific ESCALAB 250 Xi) and Raman spectroscopy using a Witec Alpha 300 R analyzer were employed to analyze the surface elemental composition and vibrational modes of the samples, respectively. The surface topography of the samples was examined using a scanning electron microscope (SEM, Carl Zeiss AG Ultra-55), while a transmission electron microscope (TEM, JEOL JEM-2100 F) combined with energy-dispersive X-ray spectroscopy (EDS) to examine structural evolution and elemental distribution.

Electrochemical measurements: Electrochemical measurements were performed in a three-electrode system using a CHI 760 E electrochemical workstation (Shanghai Chenhua Instrument Co., Ltd.). A (Fe^{3+}, PO_4^{3-})-$Ni(OH)_2$/NiOOH working electrode (1 × 1 cm^2) was used, with Hg/HgO and a graphite rod serving as the reference electrode and counter electrode, respectively. Unless otherwise specified, the electrolyte used in the experiments was maintained at 1.0 mol/L KOH. Polarization curves were obtained via cyclic voltammetry (CV) at a scan rate of 10 mV/s. Simultaneously, all potentials were converted to reversible potentials (RHE): hydrogen gas was introduced into the three-electrode system, typically for at least half an hour, to saturate the solution near the electrodes with hydrogen; after the measurement stabilized, the potential difference between the reference electrode and the working electrode was measured, and this voltage represents the calibrated reference electrode potential. (Typically between 0.92 and 0.94); all CV polarization curves were corrected for IR compensation during measurement. IR compensation is an optimal compensation level that achieves the best curve shape while avoiding curve distortion caused by overcompensation. Chronopotentiometric (CP) testing was conducted under the same electrolyte conditions at a current density of 100 mA/cm^2, and the stability of the catalyst was evaluated.

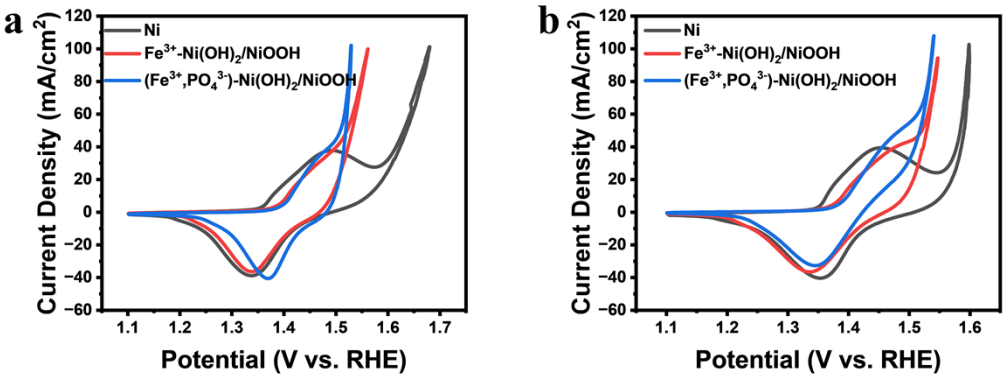

Fig. S1. Polarization curves for (a) 100 and (b) 200 scan intervals before and after electrochemical oxidation.

To investigate the mechanism of electrochemical oxidation, the cyclic voltammetry (CV) scan segment (0.1 mM Fe^{3+}, 10 mM PO_4^{3-}) was systematically adjusted during the OER evaluation. In terms of enhancing OER performance, the 100-cycle extended oxidation process (Fig. S1a) outperformed the 200-cycle process (Fig. S1b). Since the duration of electrochemical oxidation primarily determines the extent of PO_4^{3-} modification and lays the foundation for subsequent synergistic effects with Fe^{3+}, we selected the 100-cycle process as the control group for electrochemical oxidation time.

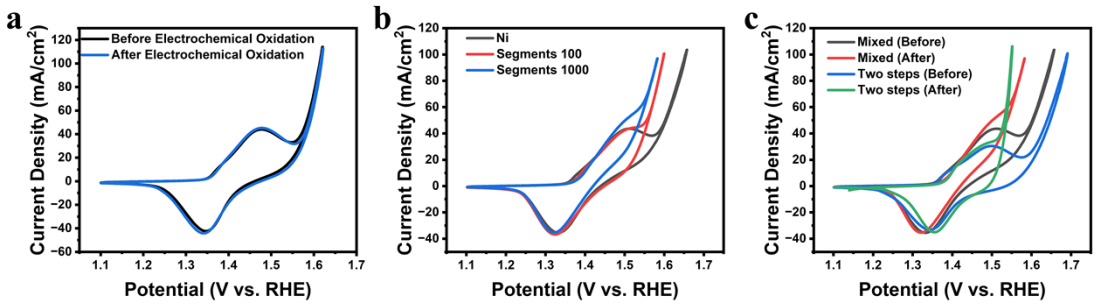

Fig. S2. Polarization curves for (a) before and after 5 mM PO_4^{3-} electrochemical oxidation, (b) before and after electrochemical oxidation with 100 and 1000 scan segments in the mixed electrolyte containing 0.1 mM Fe^{3+} and 5 mM PO_4^{3-}, and (c) comparison of performance enhancement before and after one-step electrochemical oxidation in mixed electrolyte and two-step stepwise electrochemical oxidation.

To verify the necessity of our two-step stepwise electrochemical oxidation strategy and elucidate the synergistic effect between Fe^{3+} doping and PO_4^{3-} surface modification, we have two sets of critical control experiments. The first control group is sole PO_4^{3-} electrochemical oxidation on bare Ni mesh without pre-Fe^{3+} doping, and the results show that the OER performance of bare Ni mesh is nearly unchanged after sole PO_4^{3-} modification (Fig. S2a), which confirms that PO_4^{3-} alone cannot achieve effective enhancement of catalytic activity, and Fe^{3+} doping is a prerequisite for the subsequent functional modification of PO_4^{3-}: Fe^{3+} doping first modulates the electronic structure of the Ni-based matrix, shifting the Ni 2p characteristic peak to a higher binding energy, promoting the elevation of the Ni valence state, and thus laying an electronic foundation for the synergistic effect. The second control group is the one-step electrochemical oxidation in the electrolyte containing both Fe^{3+} and PO_4^{3-}, and we conducted CV performance comparisons under 100 and 1000 scanning segments respectively (Fig. S2b); the results show that the one-step co-modification strategy can improve the OER performance to a certain extent, but the enhancement magnitude is significantly lower than that of our two-step stepwise doping and modification method (Fig. S2c). These two sets of control experiments jointly demonstrate that only through the two-step stepwise electrochemical oxidation strategy can the synergistic effect of Fe^{3+} doping and PO_4^{3-} modification be fully exerted to realize the stepwise optimization of electronic structure and the gradual improvement of catalytic performance, which confirms the necessity and unique superiority of our stepwise modification strategy.

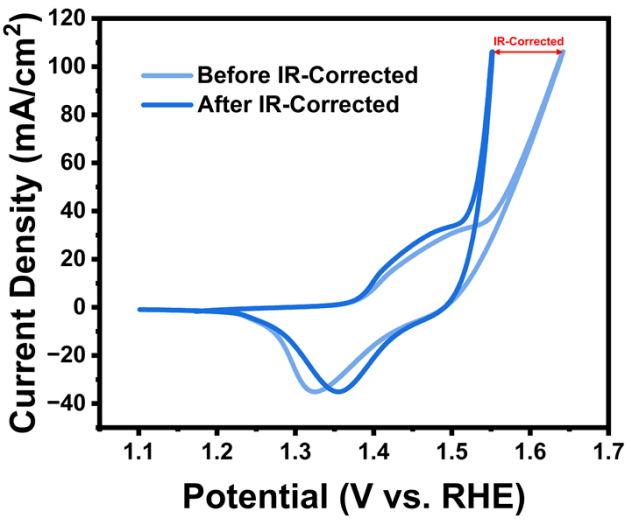

Fig. S3. CV polarization curves of (Fe^{3+}, PO_4^{3-})-$Ni(OH)_2$/NiOOH (0.1 mM Fe^{3+}, 5 mM PO_4^{3-}) before and after iR correction.

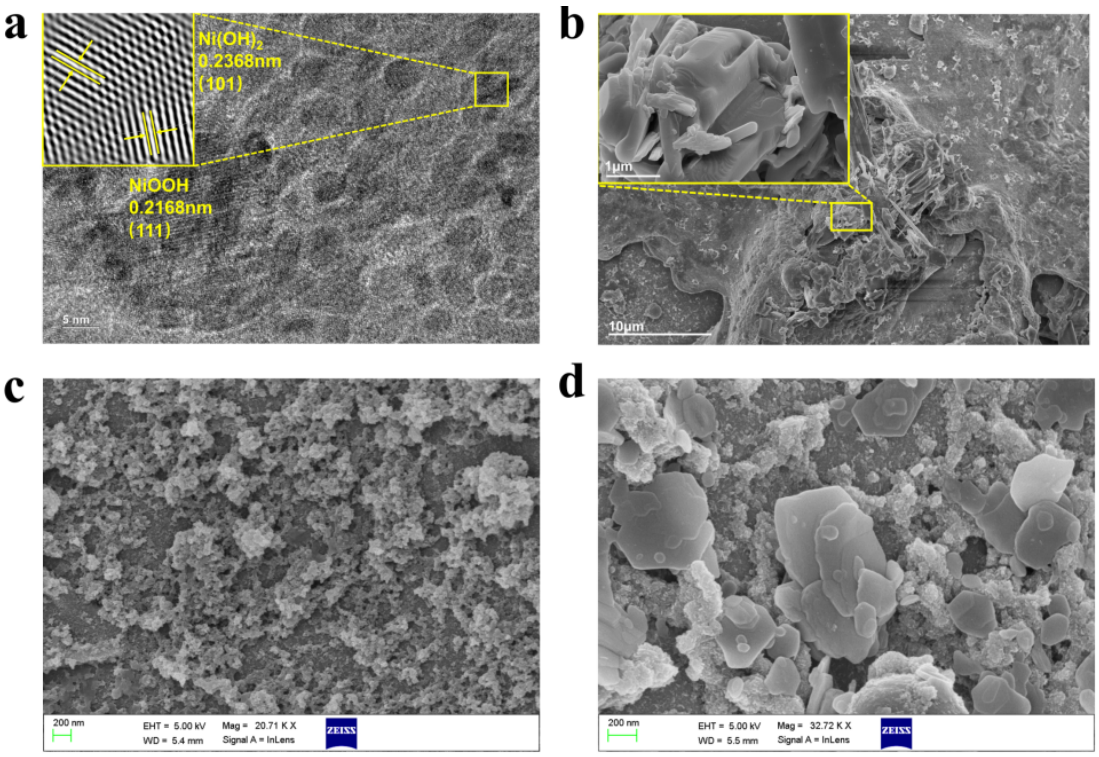

Fig. S4. (a) TEM image of (Fe^{3+}, PO_4^{3-})-$Ni(OH)_2$/NiOOH, (b, c, d) SEM image of (Fe^{3+}, PO_4^{3-})-$Ni(OH)_2$/NiOOH.

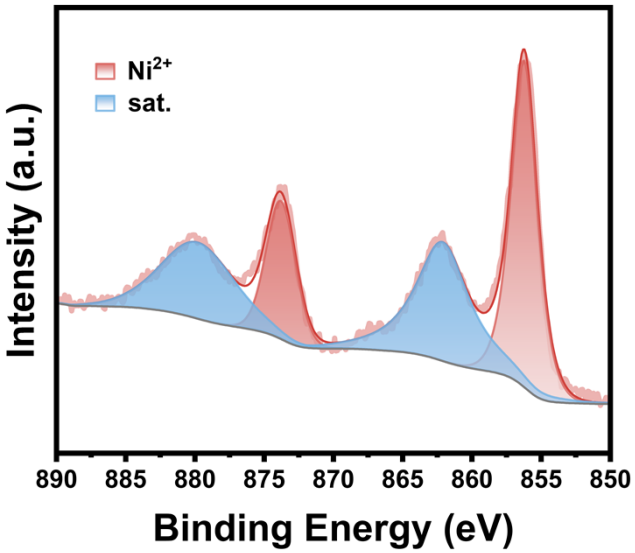

Fig. S5. Ni 2p XPS spectra of $Ni(OH)_2$/NiOOH.

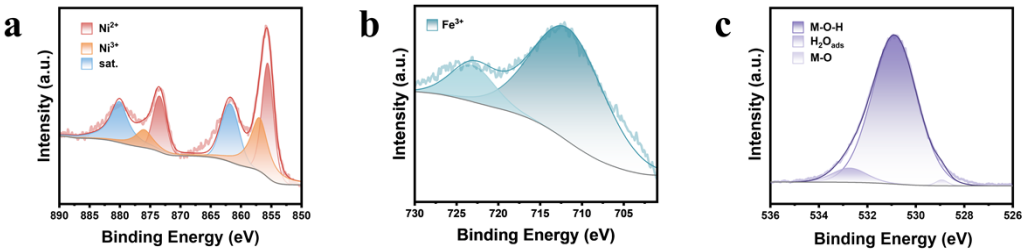

Fig. S6. (a) Ni 2p, (b) Fe 2p, (c) O 1s XPS spectra of (Fe^{3+}, PO_4^{3-})-$Ni(OH)_2$/NiOOH.

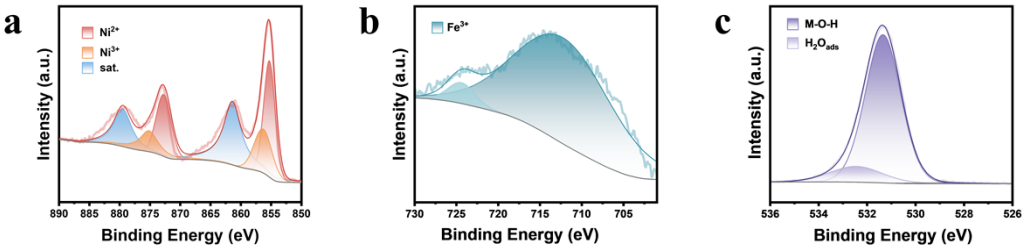

Fig. S7. (a) Ni 2p, (b) Fe 2p, (c) O 1s XPS spectra of Fe^{3+}-$Ni(OH)_2$/NiOOH.

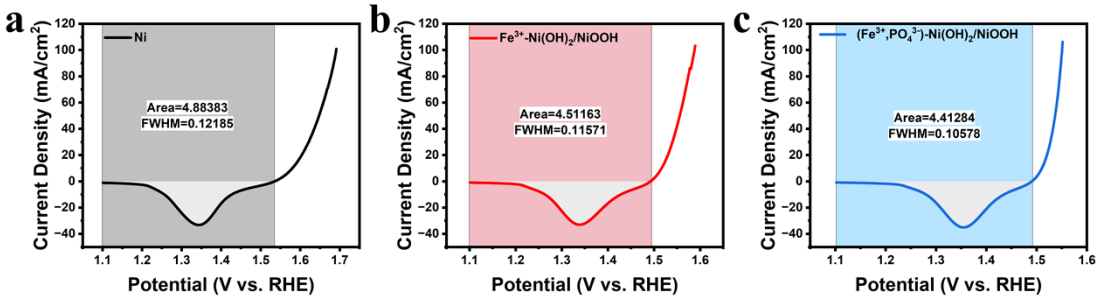

Fig. S8. Reduction peak area of cyclic voltammetry (CV) curves for (a) bare nickel mesh, (b) Fe^{3+}-$Ni(OH)_2$/NiOOH, and (c) (Fe^{3+}, PO_4^{3-})-$Ni(OH)_2$/NiOOH.

$$\sigma = \frac{S}{v \cdot e \cdot N_A}$$

Where:

- σ: molar amount of electrochemically active sites per unit electrode area, unit: $mol \cdot cm^{-2}$;
- S: integrated area of the characteristic reduction peak of Ni^{3+}/Ni^{2+} redox couple in the cyclic voltammetry (CV) curve, unit: $A \cdot V \cdot cm^{-2}$;
- v: scan rate of the CV test, unit: $V \cdot s^{-1}$;
- e: elementary charge, constant value: 1.602×10^{-19} C;
- N_A: Avogadro constant, constant value: 6.022×10^{23} mol^{-1}.

Table S1. Molar amount of electrochemically active sites per unit electrode area.

Catalytic Materials	**σ (mol · cm^{-2})**
Ni	**1.104 x 10^{-6}**
Fe^{3+}-$Ni(OH)_2$/NiOOH	**9.368 x 10^{-7}**
(Fe^{3+},PO_4^{3-})-$Ni(OH)_2$/NiOOH	**9.163 x 10^{-7}**

we adopted a quantitative electrochemical method based on cyclic voltammetry (CV) curves for calculation. In alkaline electrolyte, the reduction of NiOOH corresponds to a one-electron reversible redox reaction of $Ni^{3+} \rightarrow Ni^{2+}$, which presents a characteristic reduction peak in the CV curve. By integrating the peak area of this characteristic reduction peak, and converting the voltage axis to the time axis according to the scan rate of the CV test, we further converted the reduction peak area into the total amount of electrons involved in the reduction reaction per unit electrode area[1] (equivalent to the integration of current density over time). Based on Faraday's law, the total transferred charge is quantitatively equivalent to the amount of in-situ formed NiOOH, thus we can accurately calculate the content of NiOOH generated in situ on the electrode surface. The quantitative results show that the number of active sites of the (Fe^{3+}, PO_4^{3-})-$Ni(OH)_2$/NiOOH catalyst (Fig. S8c) remains at a similar level to that of the Fe^{3+}-$Ni(OH)_2$/NiOOH (Fig. S8b) and bare Ni mesh sample (Fig. S8a), with no significant increase observed after electrochemical oxidation. In contrast, the polarization curves show a stepwise and significant enhancement in OER performance from the bare Ni mesh, Fe^{3+}-doped sample to the final (Fe^{3+}, PO_4^{3-})-modified sample. This confirms that the performance improvement is not contributed by an increased number of active sites, but by the boosted intrinsic activity of each NiOOH active site.

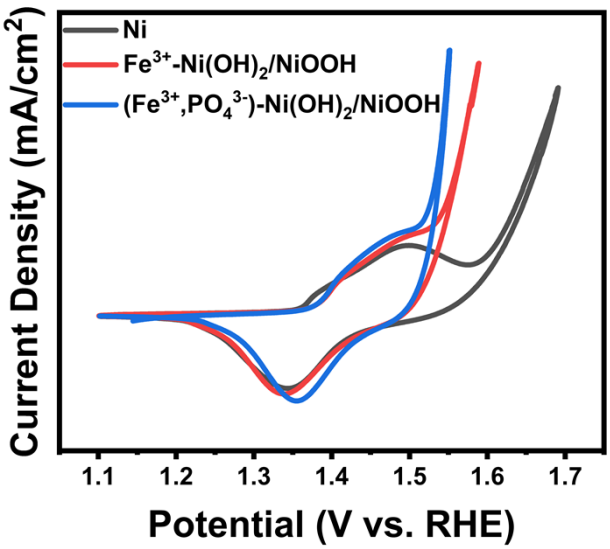

Fig. S9. CV polarization curves before and after the two-step electrochemical oxidation (0.1 mM Fe^{3+}, 5 mM PO_4^{3-}), normalized by the respective reduction peak areas of the three samples.

To further verify that the performance improvement is not contributed by an increased number of active sites, but by the boosted intrinsic activity of each NiOOH active site, we supplemented the CV polarization curves (Fig. S9) normalized by the integrated reduction peak area[2] (i.e., the total amount of active sites). The normalized curves clearly demonstrate that the (Fe^{3+}, PO_4^{3-})-$Ni(OH)_2$/NiOOH catalyst exhibits remarkably higher intrinsic OER activity than the Fe^{3+}-only doped sample and bare Ni mesh.

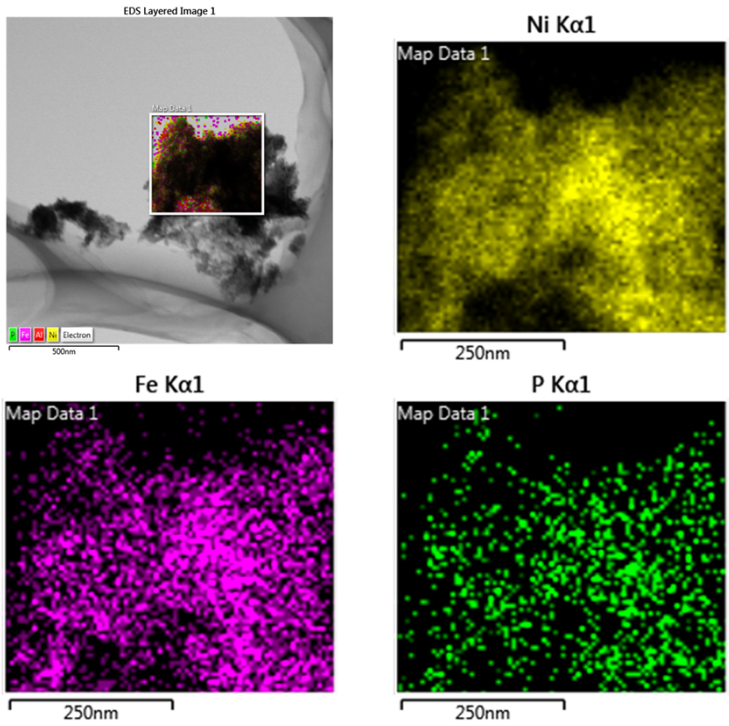

Fig. S10. EDS elemental mapping images of the (Fe^{3+}, PO_4^{3-})-$Ni(OH)_2$/NiOOH catalyst after the 100 h long-term OER stability test.

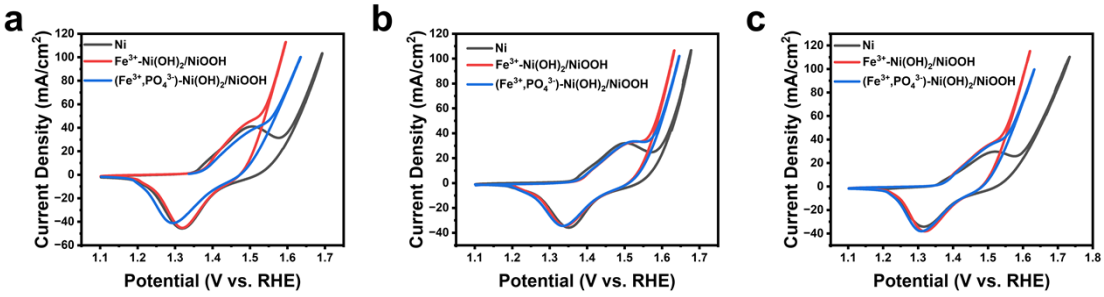

Fig. S11. CV polarization curves before and after electrochemical oxidation: (a) in the electrolyte containing 0.1 mM Fe^{3+} and 100 mM PO_4^{3-}, (b) in the electrolyte containing 0.01 mM Fe^{3+} and 5 mM PO_4^{3-}, and (c) in the electrolyte containing 1 mM Fe^{3+} and 5 mM PO_4^{3-}.

The concentration optimization was carried out via a two-step sequential screening strategy, and systematic pre-experiments were performed to determine the effective concentration range before the formal response surface optimization:

For PO_4^{3-} concentration screening: We first fixed the Fe^{3+} concentration at 0.1 mM for the first-step anodic oxidation, and performed pre-experiments with a 10-fold concentration gradient (1 mM, 10 mM, 100 mM) for the second-step PO_4^{3-} modification. The results showed that both 1 mM and 10 mM PO_4^{3-} achieved enhanced OER performance, while 100 mM PO_4^{3-} led to an obvious performance decrease after the second electrochemical oxidation (Fig. S11a). Since the performance enhancement of 1 mM PO_4^{3-} was slightly weaker than that of 10 mM, we further selected concentration points within the range of 1–10 mM to find the optimal value, and finally confirmed that 5 mM PO_4^{3-} achieved the best OER performance.

For Fe^{3+} concentration screening: We fixed the optimal PO_4^{3-} concentration of 5 mM obtained above, and adjusted the Fe^{3+} concentration in the first-step anodic oxidation, also starting with a 10-fold concentration gradient for pre-experiments. When the Fe^{3+} concentration reached 1 mM, obvious reddish-brown precipitate appeared in the electrolyte (Fig. S22), accompanied by a significant decay in OER performance after the second electrochemical oxidation (Fig. S11c); when the Fe^{3+} concentration was 0.01 mM, the OER performance also showed an obvious attenuation after the second electrochemical oxidation (Fig. S11b). We further narrowed the concentration range for optimization: at 0.2 mM Fe^{3+}, the OER performance showed a two-step enhancement, but weak precipitate was still observed in the electrolyte (Fig. S22), indicating that this concentration had reached the saturation upper limit; at 0.05 mM Fe^{3+}, the two-step performance enhancement was very weak, so this concentration was set as the lower limit of the effective range; while 0.1 mM Fe^{3+} achieved the most significant two-step performance improvement among all tested concentrations.

Based on the above systematic pre-experiments, we finally determined the effective concentration range of PO_4^{3-} as 1–10 mM and Fe^{3+} as 0.05–0.2 mM. The 3 concentration gradients for each ion in the response surface model were selected within this narrow effective range, and the experimental results have shown a clear and regular trend of performance change with concentration.

Table S2. Index Table of CV Polarization Curves Before and After Electrochemical Oxidation for Various Concentration Combinations

Fe^{3+} concentration / PO_4^{3-} concentration	**0.05 mM**	**0.1 mM**	**0.2 mM**
1 mM	Fig. S6 (5.62%)	Fig. S7 (6.95%)	Fig. S8 (2.61%)
5 mM	Fig. S9 (10.09%)	Fig. S5 (10.64%)	Fig. S10 (9.43%)
10 mM	Fig. S11 (6.84%)	Fig. S12 (9.45%)	Fig. S13 (4.28%)

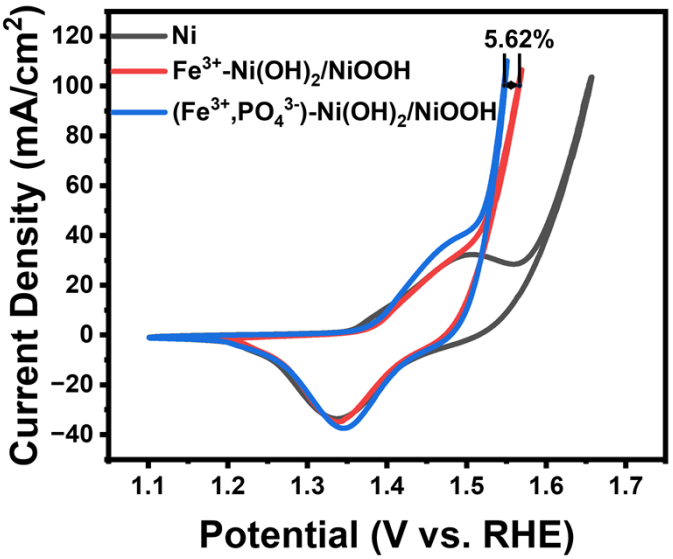

Fig. S12. Polarization curves before and after electrochemical oxidation in an electrolyte with concentrations of 0.05 mM Fe^{3+} and 1 mM PO_4^{3-}.

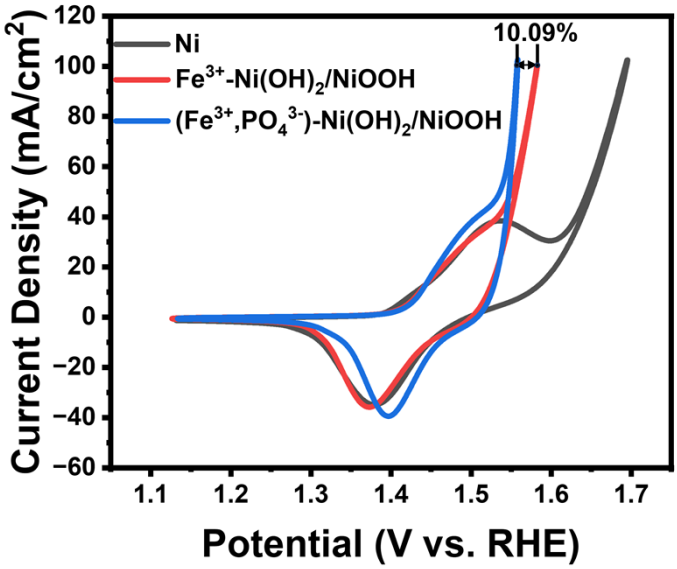

Fig. S13. Polarization curves before and after electrochemical oxidation in an electrolyte with concentrations of 0.05 mM Fe^{3+} and 5 mM PO_4^{3-}.

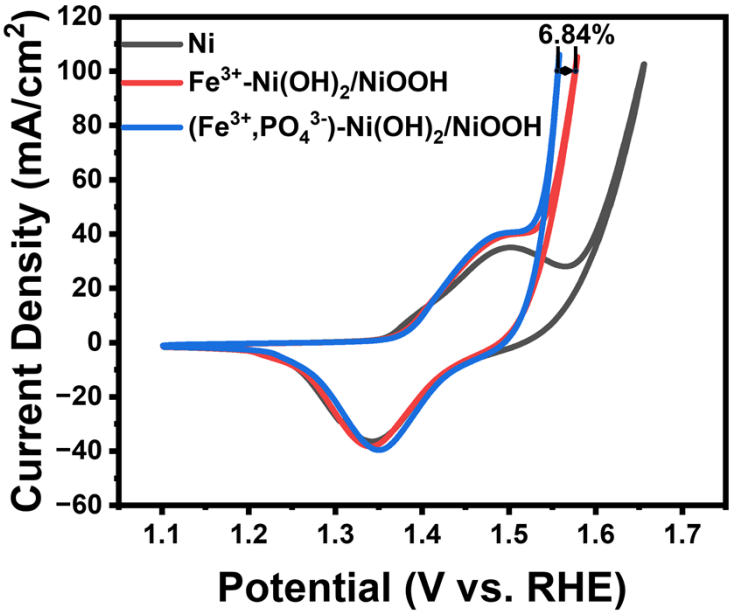

Fig. S14. Polarization curves before and after electrochemical oxidation in an electrolyte with concentrations of 0.05 mM Fe^{3+} and 10 mM PO_4^{3-}.

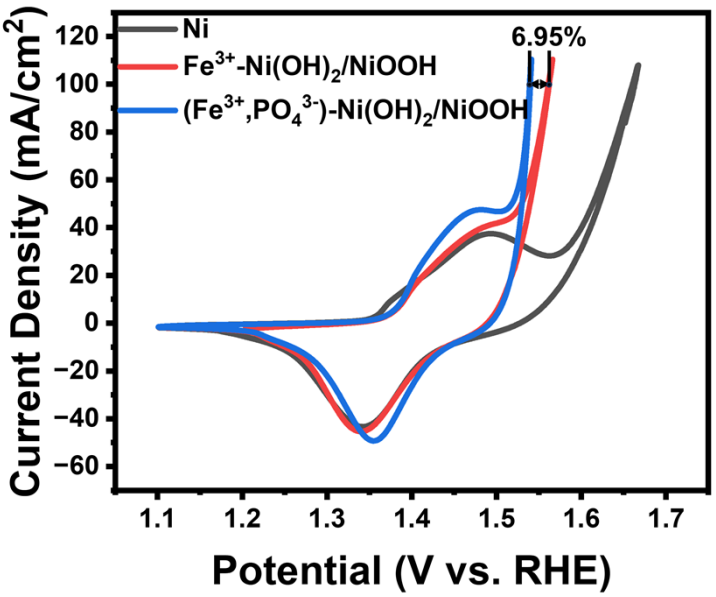

Fig. S15. Polarization curves before and after electrochemical oxidation in an electrolyte with concentrations of 0.1 mM Fe^{3+} and 1 mM PO_4^{3-}.

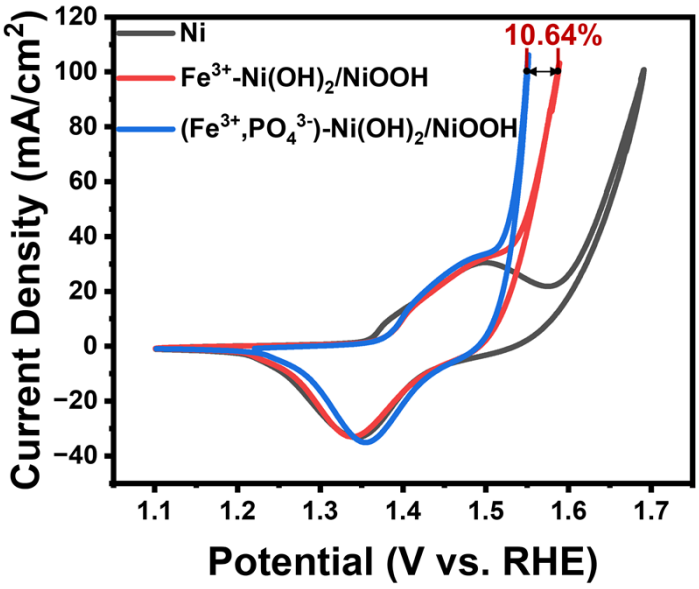

Fig. S16. Polarization curves before and after electrochemical oxidation in an electrolyte with concentrations of 0.1 mM Fe^{3+} and 5 mM PO_4^{3-}.

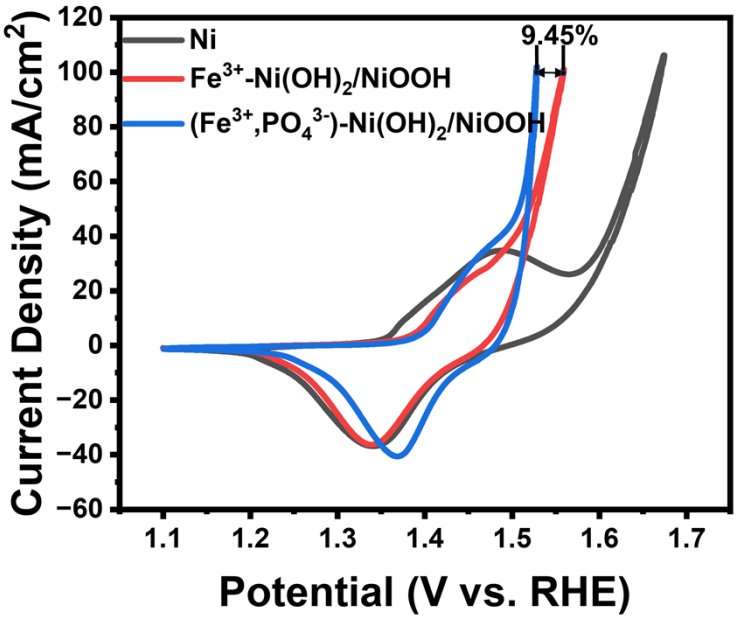

Fig. S17. Polarization curves before and after electrochemical oxidation in an electrolyte with concentrations of 0.1 mM Fe^{3+} and 10 mM PO_4^{3-}.

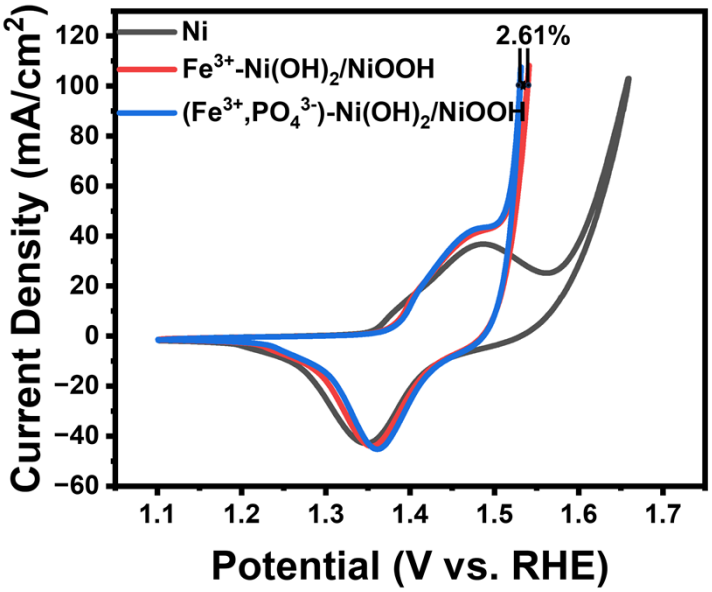

Fig. S18. Polarization curves before and after electrochemical oxidation in an electrolyte with concentrations of 0.2 mM Fe^{3+} and 1 mM PO_4^{3-}.

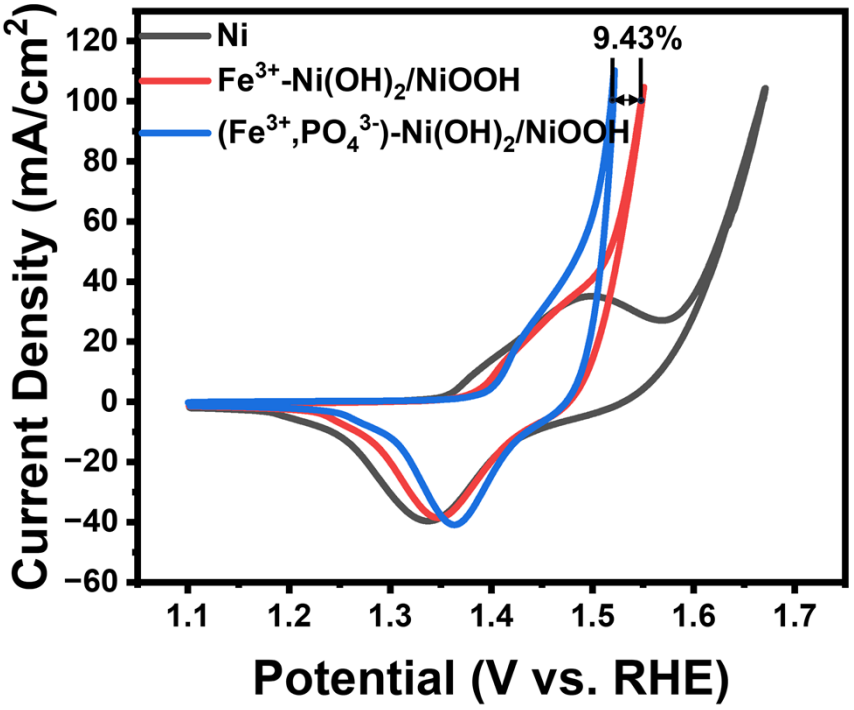

Fig. S19. Polarization curves before and after electrochemical oxidation in an electrolyte with concentrations of 0.2 mM Fe^{3+} and 5 mM PO_4^{3-}.

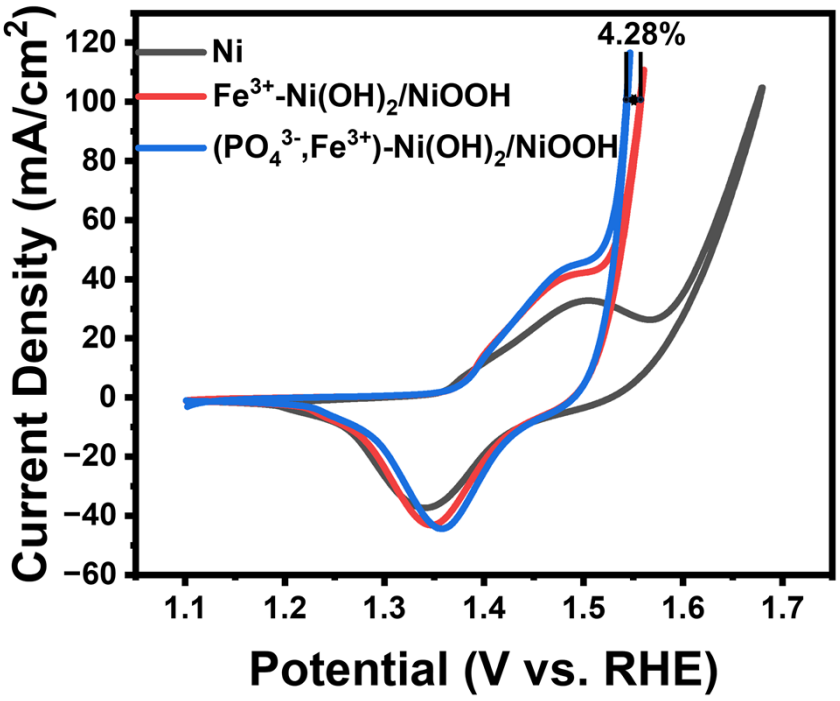

Fig. S20. Polarization curves before and after electrochemical oxidation in an electrolyte with concentrations of 0.2 mM Fe^{3+} and 10 mM PO_4^{3-}.

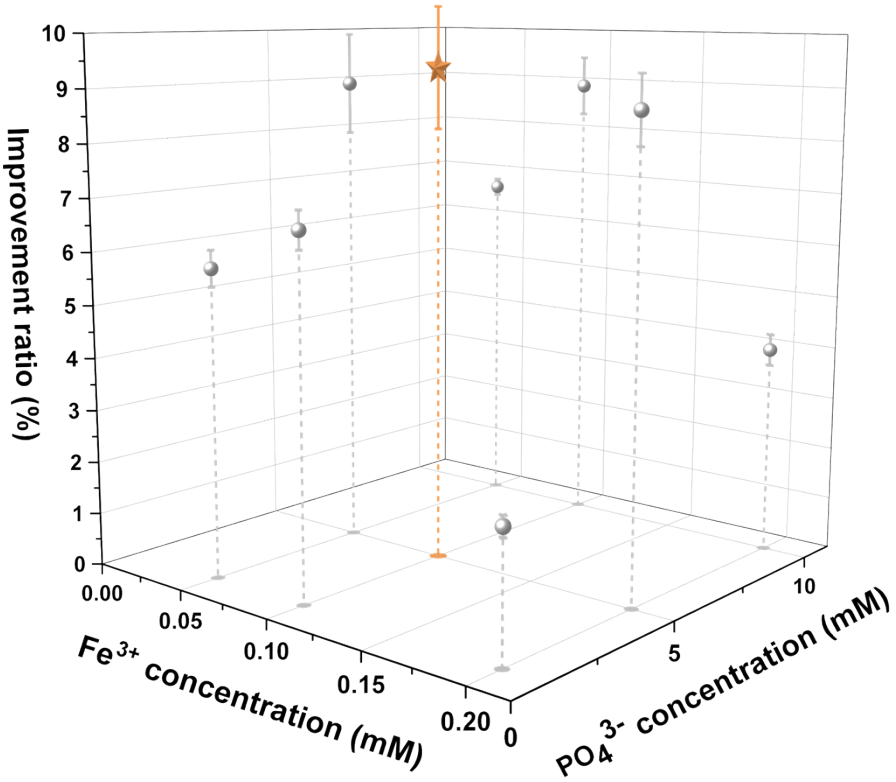

Fig. S21. 3D scatter plot of OER performance improvement ratio with complete error bars for all experimental points, versus Fe^{3+} concentration and PO_4^{3-} concentration.

Considering that the error bars would be severely obscured by the fitted curved surface in the 3D response surface plot of the main text, we did not add error bars to the figure in the main text. Instead, we have supplemented a 3D scatter plot with complete error bars (Fig. S21) (representing the standard deviation of at least three independent replicate experiments) for all experimental points.

Fig. S22. Optical photographs of $Fe(OH)_3$ precipitate formed in 1 mol/L KOH electrolyte: (a) with 1 mM Fe^{3+} addition, and (b) with 0.2 mM Fe^{3+} addition.

When the Fe^{3+} concentration exceeds the optimal value of 0.1 mM (e.g., 0.2 mM and 1 mM), the electrolyte becomes obviously turbid and reddish-brown precipitate appears, which has been confirmed by the supplemented optical photos of the electrolytes with different Fe^{3+} concentrations (Fig. S22). For the catalysts prepared in the electrolyte with $Fe(OH)_3$ precipitate, the first-step Fe^{3+} doping still achieved a certain OER performance enhancement, but the second-step PO_4^{3-} modification was significantly hindered, showing a much weaker performance improvement compared with the optimal concentration group. The only variable between these groups and the optimal group is the formation of $Fe(OH)_3$ precipitate, thus it can be confirmed that the generated $Fe(OH)_3$ phase blocks the pore structure of the catalyst layer, hinders the subsequent PO_4^{3-} surface modification, and ultimately leads to the attenuation of OER performance.

Table S3. Performance comparison of the (Fe^{3+}, PO_4^{3-})-$Ni(OH)_2$/NiOOH catalyst with previously reported Ni-based alkaline OER catalysts.

Catalyst	Overpotential (mV,10mA/cm^2)	Tafel slope (mV/dec)	Stability (h)
edge riched-NiFe LDH [3]	228	58.2	22
Fe1Ni2@ClBC [4]	259	49	40
$Ni(OH)_2$-$PMo_{11}Fe$ [5]	229	58	48
Ru@d-NiFe LDH [6]	230	35.3	120
Ru-SAC/NiFe LDH [7]	196	40	120
Co-NiFe LDH/TGF [8]	252	63.13	11.1
NiFe–BTC@CNT [9]	230	36	800
Ni3S2-Co9S8@NiFe LDH-Vo [10]	190	42	100
NixFey/GO [11]	273	51.45	60
(Fe^{3+},PO_4^{3-})-$Ni(OH)_2$/NiOOH	168	28	100

References

1 E. K. Volk, M. E. Kreider, D. M. Gibson Colón, M. Müller, S. Sunde, S. M. Alia and S. Kwon, ACS Catal., 2025, 15, 11475–11486.

2 X. Zhang, Z. H. Wang, S. Liu, M. T. Lu, Y. Y. Wang, B. L. Luo, T. Shen, Z. Y. Ren, Z. M. Chen and B. Liu, ACS Appl. Mater. Interfaces, 2025, 17, 13851–13860.

3 R. Zhang, Q. Wu, Y. Han, Y. Zhang, X. Wu, J. Zeng, K. Huang, A. Du, J. Chen, D. Zhou and X. Yao, Small, 2025, 21, 2408266.

4 J. T. Li, K. T. Zheng, C. Zhang, L. Jiao, Z. H. Dong, X. Y. Tao, R. Su, H. J. Xie and C. J. Xu, Chem. Eng. J., 2023, 462, 142267.

5 Z. R. Wang, Q. H. Ye, W. C. Chen, Y. L. Zhao, X. J. Cao, W. X. Shi and P. L. He, Adv. Funct. Mater., 2026, 36, e11187.

6 S. H. Wang, M. L. Fan, H. F. Pan, J. H. Lyu, J. S. Wu, H. L. Tang and H. N. Zhang, J. Energy Chem., 2024, 96, 526–535.

7 M. Israr, S. Ali, J. Q. Zhang, Y. Zeng, M. Humayun, H. Yu, X. Chen, C. Chen and Y. D. Li, Small, 2025, 21, 2500828.

8 D. N. Li, X. Shao, M. M. Umair, F. B. Hou, S. Li, Y. M. Tang, L. M. Cao and J. Yang, Int. J. Hydrogen Energy, 2024, 80, 11–21.

9 S. Cho, Y. Oh, H. T. Nguyen, K. Chae, N. A. T. Tran, Y.-W. Lee, J. Hong, D. Shin, H.-S. Cho and Y. Cho, Int. J. Hydrogen Energy, 2024, 90, 747–756.

10 Y. F. Gao, P. Cui, T. Gu and F. Miao, Int. J. Hydrogen Energy, 2025, 109, 287–294.

11 P. F. Guo, Z. Ying, J. Q. Tong, J. X. Hong, X. Y. Zheng and G. M. Cui, Int. J. Hydrogen Energy, 2025, 175, 151515.